# Crashing with disorder: Reaching the precision limit with tensor-based wavefront shaping

Rodrigo Gutiérrez-Cuevas, Dorian Bouchet, Julien de Rosny, Sébastien M. Popoff

# Crashing with disorder: Reaching the precision limit with tensor-based wavefront shaping

Rodrigo Gutiérrez-Cuevas,[1]* Dorian Bouchet,[2] Julien de Rosny,[1] and Sébastien M. Popoff[1]

[1]Institut Langevin, ESPCI Paris, Université PSL, CNRS, 75005 Paris, France
[2]Université Grenoble Alpes, CNRS, LIPhy, Grenoble, France
*rodrigo.gutierrez-cuevas@espci.fr

24 July 2023

**Perturbations in complex media, due to their own dynamical evolution or to external effects, are often seen as detrimental. Therefore, a common strategy, especially for telecommunication and imaging applications, is to limit the sensitivity to those perturbations in order to avoid them. Here, we instead consider crashing straight into them in order to maximize the interaction between light and the perturbations and thus produce the largest change in output intensity. Our work hinges on the innovative use of tensor-based techniques, presently at the forefront of machine learning explorations, to study intensity-based measurements where its quadratic relationship to the field prevents the use of standard matrix methods. With this tensor-based framework, we are able to identify the *optimal crashing channel* which maximizes the change in its output intensity distribution and the Fisher information encoded in it about a given perturbation. We further demonstrate experimentally its superiority for robust and precise sensing applications. Additionally, we derive the appropriate strategy to reach the precision limit for intensity-based measurements leading to an increase in Fisher information by more than four orders of magnitude with respect to the mean for random wavefronts when measured with the pixels of a camera.**

When light propagates through complex media, such as biological tissue, paint, clouds or even multimode fibers (MMF), it is mixed into a high number of degrees of freedom leading to the observation of a seemingly random speckle pattern at the output [1, 2]. While the process leading to the generation of this intricate interference pattern is complex, owing to the deterministic and linear nature of the propagation of light in such media, the response of the system between a set of input and output modes is fully represented by a single matrix $\mathbf{H}$. This matrix usually corresponds to the scattering matrix or part of it, such as the transmission or reflection matrices. While its derivation from an analytical or numerical models is highly challenging and often impossible, experimentally, it can be measured via wavefront-shaping techniques [3, 4]. This matrix gives us full knowledge over the wave propagation, thus enabling many applications in imaging [2, 5–7] quantum information [8], among many others [1, 2, 9]. However, the dynamics of the system or external actions introduce perturbations into the known configuration, which render our previous knowledge approximate at best. For applications in telecommunications and imaging, the detrimental effect of this perturbation can be bypassed by finding a set of channels that are insensitive to it [10–15]. When the changes depend on a single parameter $\zeta$ these channels can be identified as generalized principal modes which are insensitive to first-order variations of $\zeta$ [11–13, 15–18].

Nonetheless, in certain scenarios, the objective may shift from mitigating the impacts of perturbations towards actively amplifying them. This is the case, for example, when we want to use the output light for sensing applications [18–24]. By enhancing the interaction between the propagating light and the perturbation, the output field becomes more sensitive to the perturbation and thus carries more information about it, usually quantified by the Fisher information $\mathcal{J}$. This increase in information allows for increasing the precision when estimating small changes in $\zeta$, according to the Cramér-Rao bound, which states that the variance of the estimation $\sigma_\zeta^2$ will be larger or equal to the reciprocal of the Fisher information, i.e. $\sigma_\zeta^2 \geq \mathcal{J}^{-1}$ [25, 26]. When one uses an external reference to access both the amplitude and phase of the output field, the channel maximizing the Fisher information carries almost all the information in its global phase [18]. This presents a significant constraint, since phase measurements in optics are highly susceptible to noise, and require a level of stability usually only available in laboratory conditions, making such an approach less suitable for real-life implementations. In comparison, protocols based on intensity measurements are quite robust and therefore broadly applicable [21–24]. In particular, the spatial information concealed within the speckle pattern of the light coming out of a complex medium has been exploited to develop a wide range of specklegram sensing devices [21–24]. However, the identification of the channel maximizing the information carried by its output intensity distribution, and the derivation of the strategy that allows reaching the precision limit remain unsolved. This is in part due to the fact that the relation between the input field and the output intensity distribution is not linear, but rather quadratic which prevents the use of standard matrix methods.

To solve these problems, we exploit the versatility of higher-order tensors to describe the quadratic relationship between the input field and its output intensity distribution. We use this tensor-based framework to study three practical configurations for robust intensity-based sensing applications. First, when we only have control over the input wavefront for a fixed detection scheme at the distal end of the fiber. Second, when controlling the projection of the outgoing field on the distal end for a fixed arbitrary input. Third, when controlling both the input wavefront and the output projections. In particular, we experimentally study the case of an MMF which is perturbed by pressing down on it transversally with a motorized actuator as exemplified in Fig. 1a. The parameter $\zeta$ represents the linear displacement of the actuator and $\mathbf{H}$ the transmission matrix (TM) between the input modes formed by the 144 modes of the fiber (see Methods for more details), and a set of

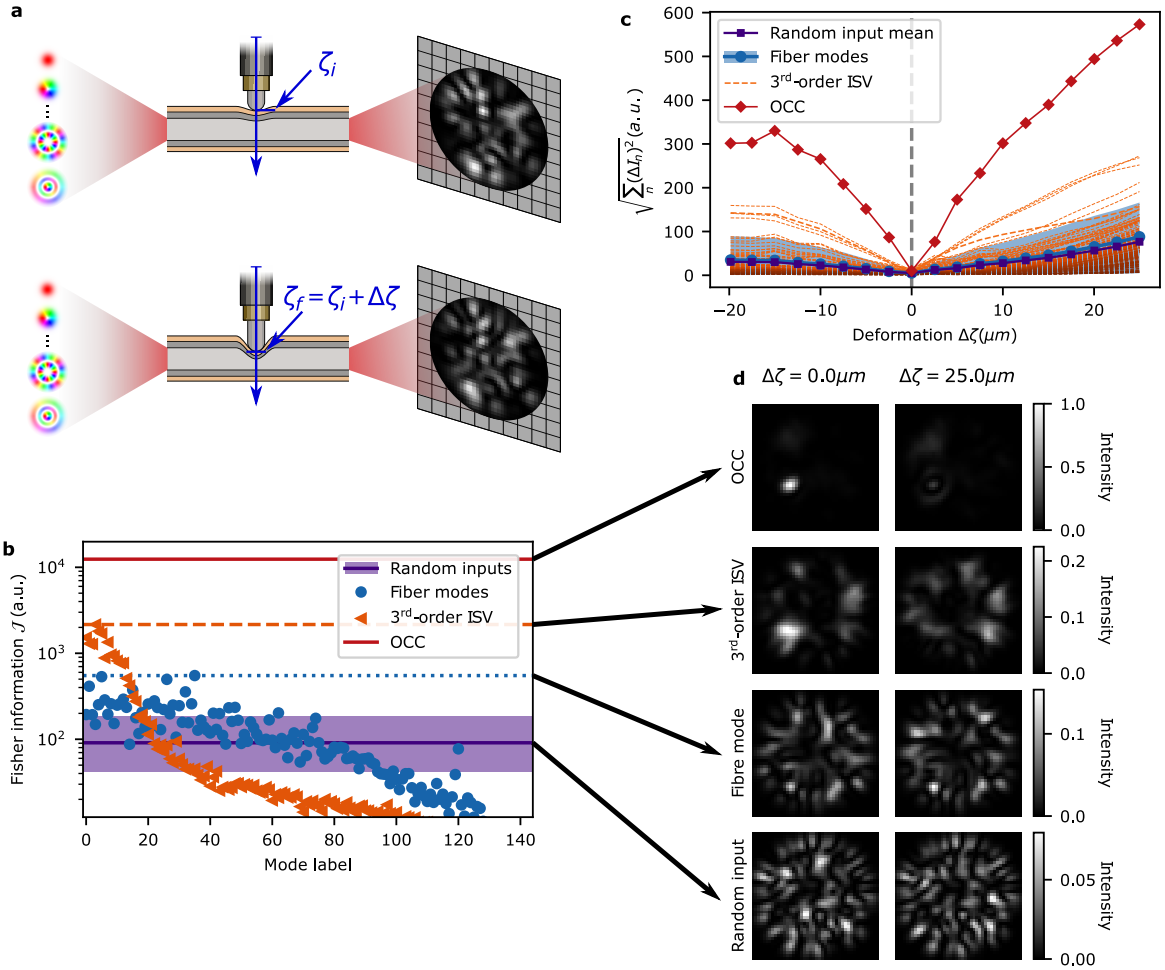


**Figure 1 | Sensitivity to perturbations.** **a**, Change on the output intensity distribution induced by a local deformation on a MMF. **b**, Fisher information in the pixel basis for random inputs (where the line denotes the mean value for one-thousand states and the shaded region the range obtained), the fiber modes (where the dotted line marks the maximum value), the third-order input singular vectors (ISVs) (where the dashed line marks the maximum value), and the optimal crashing channel (OCC). **c**, Intensity change over large deformations for the same modes as in (**b**). For the random inputs only the mean is shown, and for the fiber modes the marked line denotes the mean and the shaded region the range of values. **d**, Output intensity distribution for the OCC, the most sensitive third-order ISV, the most sensitive fiber mode, as well as a random input for the reference deformation $\Delta\zeta = 0\mu m$ and a large deformation for which $\Delta\zeta = 25\mu m$.

output modes, such as the pixels of a camera. With this implementation we are able to demonstrate an enhancement in the Fisher information by more than four orders of magnitude when using the optimal input-output configuration.

## Results

### Optimizing the input field

Intuitively, the channel maximizing the Fisher information carried by its output intensity distribution, under the assumption of Gaussian noise with a known standard deviation $\sigma$, is the one for which first-order variations in $\zeta$ lead to the largest change in its output intensity distribution. Therefore, this channel can be seen as crashing straight into the perturbation, and thus we refer to it as the *optimal crashing channel* (OCC). The assumption of Gaussian noise is quite general encompassing all systems for which the noise fluctuations are dominated by dark and readout noise.

Given the quadratic dependence of the intensity on the field, one may think that there is no other choice than to cast this problem as a standard nonlinear optimization problem [14, 27, 28]. Nevertheless, higher-order tensors, which are multidimensional extensions of matrices, provide fresh perspectives in tackling intricate and nonlinear challenges [29–36]. In fact, as shown in the Methods, for a fixed set of output modes (such as the pixels of a camera) it is possible to rewrite the Fisher information as

$$\mathcal{J}(\zeta) = \frac{1}{\sigma^2}\langle \boldsymbol{\mathcal{W}}^{(3)}, \mathbf{a}\otimes\mathbf{e}^{(\mathrm{in})}\otimes\mathbf{e}^{(\mathrm{in})*}\rangle^2, \tag{1}$$

which is the inner product between the third-order tensor $\boldsymbol{\mathcal{W}}^{(3)}$, defined component-wise as $\mathcal{W}^{(3)}_{ijk} = \partial_\zeta(\mathrm{H}^*_{ij}\mathrm{H}_{ik})$ where $\mathrm{H}_{ij}$ are the components of the matrix $\mathbf{H}$, and the rank-one third-order tensor $\mathbf{a}\otimes\mathbf{e}^{(\mathrm{in})}\otimes\mathbf{e}^{(\mathrm{in})*}$ where $\mathbf{a}$ is a normalized real vector quantifying the change in the output intensity of the input field $\mathbf{e}^{(\mathrm{in})}$ over the output modes and $\otimes$ denotes the outer product (see Methods for more details). Maximizing $\mathcal{J}$ for a fixed amount of total energy at the input is equivalent to finding the best rank-one approximation of $\boldsymbol{\mathcal{W}}^{(3)}$, that is, the set of three vectors that best approximate it [33, 35].

For matrices, which are second-order tensors, finding the best rank-one approximation is a simple task achieved by com-

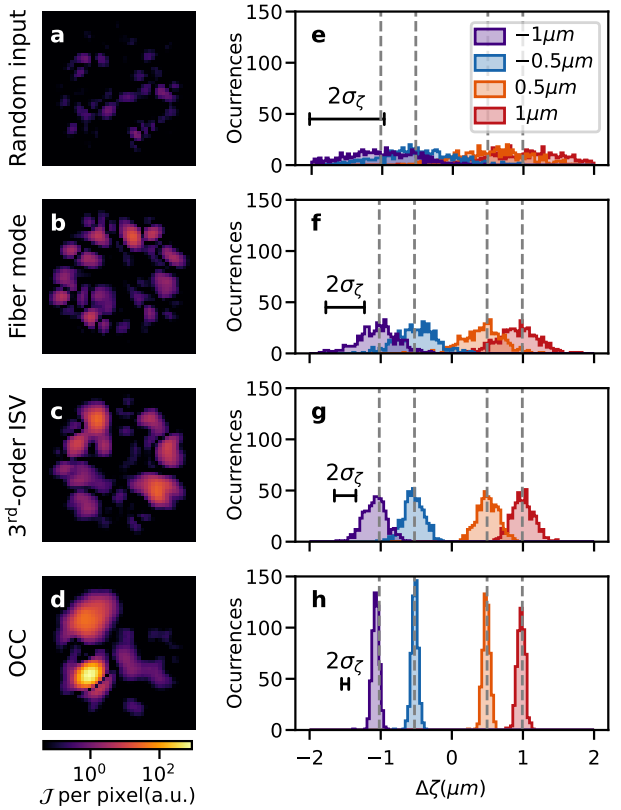


**Figure 2 | Estimating a change in the perturbation.** **a**-**d** Measured Fisher information per output pixel. **e**-**h** Histograms of estimated changes in the deformation for four different values ($\Delta\zeta = -1, -0.5, 0.5, 1\mu m$) marked with dashed gray lines and with the mean width $2\sigma_\zeta$ marked in black. Both types of plots are shown for a random input (**a**, **e**), the most sensitive fiber mode (**b**, **f**), the optimal third-order ISV (**c**, **g**), and the OCC (**d**, **h**).

puting the singular-value decomposition (SVD) and taking the outer product of the first pair of singular vectors. For higher-order tensors, however, the answer is not so simple. Nonetheless, a step in the right direction can be taken by performing the higher-order SVD (HOSVD) [31–33]. This generalization of the matrix SVD allows decomposing a higher-order tensor in terms of a sum of rank-one tensors composed of higher-order singular vectors which form orthonormal bases for their respective spaces.

To find the third-order input singular vectors (ISVs) of $\mathcal{W}^{(3)}$ we first construct this tensor from two measurements of $\mathbf{H}$, using the pixels of a camera as output modes, around a reference value $\zeta = \zeta_i$ for the deformation, and then compute its HOSVD. In Fig. 1b we compare the values of the Fisher information obtained for the third-order ISV with those obtained when using the fiber modes and one-thousand random wavefronts as inputs. It can be seen that the Fisher information for the first third-order ISVs is above all the values obtained with the fiber modes and random wavefronts, and with the maximum value being an order of magnitude larger the maximum value attained for a random wavefront. Therefore, the HOSVD immediately provides us with a set of modes generally ordered from the one with the largest Fisher information to the smallest, and with the first ones being highly sensitive to the perturbation.

*Optimal crashing channel.* One of the main differences between the HOSVD and the SVD is that the first singular vectors do not immediately provide us with the best rank-one approximation. Nonetheless, they form a reasonably good first guess that can be used as a seed for a modified version of the iterative alternating-least squares algorithm [33, 35] to determine the best rank-one approximation (see Methods for details). This allows us to identify the OCC which provides a two order of magnitude boost in Fisher information with respect to an average random wavefront, as shown in Fig. 1b.

It is also worth noting that, as seen in Fig. 1c, both the third-order ISVs and the OCC maintain their high sensitivity over a large range of deformations. However, by looking at the intensity distributions in Fig. 1d, it can be seen that their behavior is quite different. While the intensity distribution for the most sensitive third-order ISV changes radically, for the OCC it is mostly the total intensity that suffers the largest change and not the overall distribution. This feature of the OCC is a consequence of the non-unitarity of the matrix $\mathbf{H}$ for MMF which can be potentially very useful for practical implementations. Indeed, such a change can be recorded by a single detector, thus minimizing the cost of the system and allowing high-speed operations. Another feature worth noting is that the intensity distribution of the OCC is mostly concentrated around a focal spot. This allows it to focus as much information across a few pixels in order to increase the signal-to-noise ratio (SNR). Despite the similarity, the OCC is not equivalent to the channel obtained through phase conjugation to focus at the same spot [4] and for which the Fisher information value is much lower.

*Estimating the perturbation.* A direct application of the OCC regards the estimation of changes in the perturbation $\Delta\zeta$. Assuming $\Delta\zeta$ to be small, when compared to the deformation that decorrelates the output, we can safely assume a linear model for which we only need to perform calibration measurements for the reference intensity distribution and its derivative with respect to $\zeta$ above the noise level. Figures 2a-d show the Fisher information per output pixel obtained from these calibration measurements for four different input fields, namely, a random wavefront, the fiber mode with the highest Fisher information, the third-order ISV with the highest Fisher information and the OCC. Here, the drastic enhancement provided by the OCC can be appreciated. For the actual estimation, we use these same four fields but perform the measurements at a lower input power and for the four smaller deformation values $\Delta\zeta = -1, -0.5, 0.5,$ and $1\mu m$. We measure 500 intensity distributions for each field and each deformation, and use each one of these measurements to estimate the deformation (see Methods for more details). The results are shown in Figs. 2e-h. For the random input, it is practically impossible to discriminate the four peaks corresponding to the four different deformation values. For the fiber mode and the third-order ISVs, we can clearly discern the deformations that are further apart as the distributions are narrower. However, there is still significant overlap between the ones that are closer together. Finally, when we take a look at the results for the OCC, we can appreciate four well-defined peaks with a standard deviation that is more than an order of magnitude smaller than the one obtained for the random input, in agreement with the Cramér-Rao lower bound.

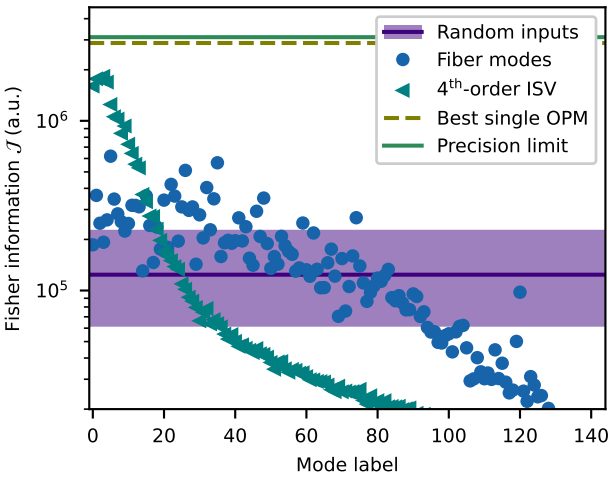


**Figure 3 | Reaching the precision limit.** Effect of using the optimal output projection modes (OPMs) on the Fisher information per photon for various input fields. It shows the Fisher information obtained when using the optimal OPMs for each of the random inputs used in Fig. 1, the fiber modes, and the fourth-order ISVs. Also shown are the Fisher information values attained for the optimal input-output combination, which defines the precision limit for intensity-based measurements, and for the optimal channel when a single OPM is being used at the output.

## Optimizing the output projection modes

One consequence of the quadratic relationship between the input field and the measured output intensity is that the Fisher information is not invariant under changes of the output modes. While the pixels of a camera might be the simplest output modes to implement experimentally, they are generally not the optimal choice since they are blind to the information that could be hidden in the relative phase variations of the field from one pixel to another, and they spread out the information across many modes, thus decreasing the SNR. To address both of these issues we could foresee demultiplexing the output field into a specifically designed set of spatial channels, which is experimentally feasible using photonic lanterns or multiplane light converters [37–39]. This is the principle behind techniques that allow increasing the information transfer for telecommunication applications [40, 41] or beating Rayleigh's curse when imaging two closely-spaced sources [42–45].

Mathematically, this spatial demultiplexing is performed by projecting the output field onto an orthogonal set of $Q$ output projection modes (OPMs), where $Q$ can smaller than the number of output modes used to define $\mathbf{H}$. If we assume that the input field is fixed, then, as shown in the Methods, the Fisher information can be rewritten as

$$\mathcal{J}(\zeta) = \frac{1}{\sigma^2}\sum_{q=1}^{Q}\langle \mathbf{p}_q, \mathbf{E}_\zeta \cdot \mathbf{p}_q\rangle^2, \tag{2}$$

where $\mathbf{p}_q$ is the $q^{\text{th}}$ OPM, and $\mathbf{E}_\zeta = \partial_\zeta\left(\mathbf{e}^{(\text{out})} \otimes \mathbf{e}^{(\text{out})*}\right)$ is a rank-2 Hermitian matrix. Therefore, the Fisher information can be maximized by choosing as OPMs the two eigenvectors of $\mathbf{E}_\zeta$ with nonzero eigenvalues. These two optimal OPMs are given by a simple linear combination of the output field $\mathbf{e}^{(\text{out})}$ and its derivative with respect to the parameter $\partial_\zeta \mathbf{e}^{(\text{out})}$. This is similar to the approaches taken for estimating the distance between two particles where the output field is projected on a Gaussian field, which resembles the point spread function, and higher-order Hermite-Gauss modes, which provide the derivatives [42–44].

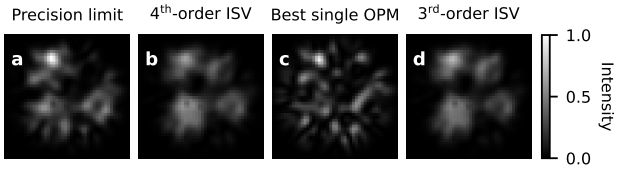


**Figure 4 | Output fields near the precision limit.** Output intensity distribution for the mode achieving the precision limit (**a**), the first fourth-order ISV (**b**), the first third-order ISV (**c**), and the best mode when using a single OPM (**d**).

Figure 3 shows the impact of projecting onto the optimal OPMs on the Fisher information for the same random inputs and fiber modes as those used in Fig. 1b. By using the optimal OPMs, the mean Fisher information obtained when using random wavefronts as inputs is an order of magnitude larger than the maximum value obtained with the OCC in the pixel basis, which clearly shows the benefits of choosing the OPMs appropriately even when one cannot control the input wavefront.

## Optimal input-output combination: reaching the precision limit

Let us now find the optimal channel when we are free to shape the input field and choose the OPMs. This optimal input-output combination is the channel that maximizes the Fisher information when projected onto its optimal OPMs, and sets the precision limit achievable with intensity measurements. To find it, we rewrite the Fisher information in terms of just two OPMs and the input field which leads to,

$$\mathcal{J}(\zeta) = \frac{1}{\sigma^2}\sum_{q=1}^{2}\langle \boldsymbol{\mathcal{W}}^{(4)}, \mathbf{p}_q^* \otimes \mathbf{p}_q \otimes \mathbf{e}^{(\text{in})} \otimes \mathbf{e}^{(\text{in})*}\rangle^2, \tag{3}$$

where we defined the fourth-order tensor $\boldsymbol{\mathcal{W}}^{(4)}$ whose components are given by $W^{(4)}_{ijkl} = \partial_\zeta(\mathrm{H}^*_{ik}\mathrm{H}_{jl})$. Even though this expression resembles the one in Eq. (1), it does not correspond to a rank-two approximation of $\boldsymbol{\mathcal{W}}^{(4)}$. Nonetheless, we can still use tensor-based techniques to obtain an excellent first guess by computing the HOSVD of $\boldsymbol{\mathcal{W}}^{(4)}$. Figure 3 shows the resulting Fisher information for the corresponding fourth-order ISVs when projected onto their respective optimal OPMs. Once more, these higher-order ISVs provide us with an ordered orthogonal basis of highly-sensitive modes, with the first ones surpassing all the modes of the fibers and random inputs.

To reach the precision limit, however, we need to perform a nonlinear optimization using the first fourth-order ISV as a seed (see Methods for details). The results shown in Fig. 3 demonstrate that the Fisher information achieved by this channel is well over two orders of magnitude above that obtained for the OCC that uses the pixels as OPMs. Nevertheless, this maximum value is very close to that provided by the first few fourth-order ISVs. Another approach consists on taking the first fourth-order ISV as a seed to find the best rank-one approximation of $\boldsymbol{\mathcal{W}}^{(4)}$. While this does not allow us to reach the precision limit, it provides us with the optimal mode when

a single OPM is used to monitor the change of intensity at the output, that is when there is a single term in Eq. (3). As can be seen in Fig. 3, this almost allows us to reach the precision limit, for which the Fisher information value is only 4.8% larger, while using a single OPM. For practical applications, it means that one can approach the precision limit within a very small margin using a single photodetector. In fact, the output fields produced by the first fourth-order ISV and the best rank-one approximation are highly similar to the one reaching the precision limit, with which they have field correlations that are above 78%. This similarity can also be appreciated in their intensity profiles, shown in Fig. 4. More surprising, however, is that the first third-order ISV obtained with the output pixel basis is also highly similar to the one reaching the precision limit (see Fig. 4). This is not intuitive since $\mathcal{W}^{(3)}$ does not contain any information about the phase at the output, which $\mathcal{W}^{(4)}$ does have.

## Outlook

By introducing tensor-based methods to the study of complex systems, we have provided a natural framework for studying intensity-based measurements. Here, we used lower-rank approximations of higher-order tensors to find the channels that are most sensitive to a given perturbation i. e. that suffer the largest change in output intensity when the perturbation changes. Their high sensitivity allows them to be used for highly robust and precise sensing applications which we demonstrated experimentally by estimating small perturbations in MMF. It was also shown that what is meant by most sensitive is highly dependent on the choice of output modes used to measure the intensity distribution. This dependence was exploited to find the channel that allows extracting the most information available at the output, and thus achieve the precision limit of intensity-based measurements.

This new framework opens the door to further investigations, such as the identification of universal input or output modes for blind parameter estimation, that is when the output modes or the input field are not known or can change over time. Additionally, the tensor-based relations established here can also be used for the study of incoherent systems where a TM cannot be derived. This last point could help gain further insight into fluorescent imaging applications through scattering media. Likewise, it can be expected for the fields presented here to find other applications, such as for focusing light inside scattering media but with properties that will be quite different when using the generalized principal modes [13].

## References


[1] S. Rotter and S. Gigan. Light fields in complex media: Mesoscopic scattering meets wave control. *Reviews of Modern Physics* **89** no. 1, p. 015 005 (2017).

[2] S. Gigan et al. Roadmap on wavefront shaping and deep imaging in complex media. *Journal of Physics: Photonics* **4** no. 4, p. 042 501 (2022).

[3] S. M. Popoff et al. Measuring the transmission matrix in optics: An approach to the study and control of light propagation in disordered media. *Phys. Rev. Lett.* **104** no. 10, p. 100 601 (2010).

[4] S. M. Popoff et al. Controlling light through optical disordered media: transmission matrix approach. *New J. Phys.* **13** no. 12, p. 123 021 (2011).

[5] S. Popoff et al. Image transmission through an opaque material. *Nat. Commun.* **1** no. 1.

[6] T. Čižmár and K. Dholakia. Exploiting multimode waveguides for pure fibre-based imaging. *Nature Communications* **3** no. 1.

[7] S. Gigan. Imaging and computing with disorder. *Nature Physics* **18** no. 9, pp. 980–985 (2022).

[8] B. Courme et al. Manipulation and certification of high-dimensional entanglement through a scattering medium. *PRX Quantum* **4** no. 1, p. 010 308 (2023).

[9] J. Hüpfl et al. Optimal cooling of multiple levitated particles through far-field wavefront shaping. *Physical Review Letters* **130** no. 8, p. 083 203 (2023).

[10] C. K. Mididoddi et al. Threading light through dynamic complex mediaE-print.

[11] S. Fan and J. M. Kahn. Principal modes in multimode waveguides. *Optics Letters* **30** no. 2, p. 135 (2005).

[12] J. Carpenter, B. J. Eggleton and J. Schröder. Observation of eisenbud–wigner–smith states as principal modes in multimode fibre. *Nature Photonics* **9** no. 11, pp. 751–757 (2015).

[13] P. Ambichl et al. Focusing inside disordered media with the generalized wigner-smith operator. *Phys. Rev. Lett.* **119** no. 3, p. 033 903 (2017).

[14] P. Ambichl et al. Super- and anti-principal-modes in multimode waveguides. *Physical Review X* **7** no. 4, p. 041 053 (2017).

[15] M. W. Matthès et al. Learning and avoiding disorder in multimode fibers. *Phys. Rev. X* **11** no. 2, p. 021 060 (2021).

[16] E. P. Wigner. Lower limit for the energy derivative of the scattering phase shift. *Physical Review* **98** no. 1, pp. 145–147 (1955).

[17] S. Rotter, P. Ambichl and F. Libisch. Generating particlelike scattering states in wave transport. *Physical Review Letters* **106** no. 12, p. 120 602 (2011).

[18] D. Bouchet, S. Rotter and A. P. Mosk. Maximum information states for coherent scattering measurements. *Nature Physics* **17** no. 5, pp. 564–568 (2021).

[19] K. Hill and G. Meltz. Fiber bragg grating technology fundamentals and overview. *Journal of Lightwave Technology* **15** no. 8, pp. 1263–1276 (1997).

[20] J. Juarez et al. Distributed fiber-optic intrusion sensor system. *Journal of Lightwave Technology* **23** no. 6, pp. 2081–2087 (2005).

[21] B. Redding, S. M. Popoff and H. Cao. All-fiber spectrometer based on speckle pattern reconstruction. *Optics Express* **21** no. 5, p. 6584 (2013).

[22] A. G. Leal-Junior et al. Optical fiber specklegram sensors for mechanical measurements: A review. *IEEE Sensors Journal* **20** no. 2, pp. 569–576 (2020).

[23] R. K. Gupta et al. Deep learning enabled laser speckle wavemeter with a high dynamic range. *Laser & Photonics Reviews* **14** no. 9, p. 2000 120 (2020).

[24] T. D. Cabral et al. Multimode exposed core fiber specklegram sensor. *Optics Letters* **45** no. 12, p. 3212 (2020).

[25] S. K. Sengupta and S. M. Kay. Fundamentals of statistical signal processing: Estimation theory. *Technometrics* **37** no. 4, p. 465 (1995).

[26] P. Réfrégier. *Noise Theory and Application to Physics* (Springer New York, 2004). doi:10.1007/978-0-387-22526-5.

[27] D. Bouchet, R. Carminati and A. P. Mosk. Influence of the local scattering environment on the localization precision of single particles. *Phys. Rev. Lett.* **124**, p. 133 903 (2020).

[28] D. Bouchet, J. Seifert and A. P. Mosk. Optimizing illumination for precise multi-parameter estimations in coherent diffractive imaging. *Opt. Lett.* **46** no. 2, pp. 254–257 (2021).

[29] L. R. Tucker. Some mathematical notes on three-mode factor analysis. *Psychometrika* **31** no. 3, pp. 279–311 (1966).

[30] L. D. Lathauwer, B. D. Moor and J. Vandewalle. On the best rank-1 and rank-$(r_1, r_2, \ldots, r_n)$ approximation of higher-order tensors. *SIAM Journal on Matrix Analysis and Applications* **21** no. 4, pp. 1324–1342 (2000).

[31] L. D. Lathauwer, B. D. Moor and J. Vandewalle. A multilinear singular value decomposition. *SIAM Journal on Matrix Analysis and Applications* **21** no. 4, pp. 1253–1278 (2000).

[32] P. Comon, X. Luciani and A. L. F. de Almeida. Tensor decompositions, alternating least squares and other tales. *Journal of Chemometrics* **23** no. 7-8, pp. 393–405 (2009).

[33] T. G. Kolda and B. W. Bader. Tensor decompositions and applications. *SIAM Review* **51** no. 3, pp. 455–500 (2009).

[34] T. G. Kolda and J. R. Mayo. An adaptive shifted power method for computing generalized tensor eigenpairs. *SIAM Journal on Matrix Analysis and Applications* **35** no. 4, pp. 1563–1581 (2014).

[35] N. D. Sidiropoulos et al. Tensor decomposition for signal processing and machine learning. *IEEE Transactions on Signal Processing* **65** no. 13, pp. 3551–3582 (2017).

[36] S. Rabanser, O. Shchur and S. Günnemann. Introduction to tensor decompositions and their applications in machine learning (2017). doi:10.48550/ARXIV.1711.10781.

[37] N. K. Fontaine et al. Geometric requirements for photonic lanterns in space division multiplexing. *Opt. Express* **20** no. 24, p. 27 123 (2012).

[38] G. Labroille et al. Efficient and mode selective spatial mode multiplexer based on multi-plane light conversion. *Opt. Express* **22** no. 13, p. 15 599 (2014).

[39] N. K. Fontaine et al. Laguerre-gaussian mode sorter. *Nature Communications* **10** no. 1.

[40] N. Bozinovic et al. Terabit-scale orbital angular momentum mode division multiplexing in fibers. *Science* **340** no. 6140, pp. 1545–1548 (2013).

[41] I. Cristiani et al. Roadmap on multimode photonics. *Journal of Optics* **24** no. 8, p. 083 001 (2022).

[42] M. Tsang, R. Nair and X.-M. Lu. Quantum theory of superresolution for two incoherent optical point sources. *Phys. Rev. X* **6** no. 3, p. 031 033 (2016).

[43] M. Paúr et al. Achieving the ultimate optical resolution. *Optica* **3** no. 10, p. 1144 (2016).

[44] K. Liang, S. A. Wadood and A. N. Vamivakas. Coherence effects on estimating two-point separation. *Optica* **8** no. 2, p. 243 (2021).

[45] N. Treps et al. Surpassing the standard quantum limit for optical imaging using nonclassical multimode light. *Physical Review Letters* **88** no. 20, p. 203 601 (2002).

## Methods

### Fisher information for intensity measurements.

Given a random process determined by a probability mass function $P(\chi|\zeta)$ for the set of random variables $\chi$ and with parametric dependence on $\zeta$, the Fisher information for the parameter $\zeta$ is defined as

$$\mathcal{J}(\zeta) = \overline{\left[\partial_\zeta \ln P(\chi|\zeta)\right]^2}, \tag{4}$$

where the overline denotes the expected values over all the possible values of $\chi$. Here, $P(\chi|\zeta)$ represents the inaccuracy of the measured the intensity distribution over the $N$ output modes $\{\mathbf{y}_1, \ldots, \mathbf{y}_N\}$ due to the presence of noise. Thus, the measured intensity distribution is given by $\chi = \mathbf{I} + \boldsymbol{w}$ where $\mathbf{I} = |\mathbf{e}^{(\text{out})}|^2$ is the expected intensity distribution and $\boldsymbol{w}$ represents the noise which is assumed to be Gaussian with known standard deviation $\sigma_n$ for the n$^{\text{th}}$ output mode. The probability mass function can then be written as

$$P(\chi|\zeta) = \prod_{n=1}^{N} \frac{1}{\sigma_n\sqrt{2\pi}} e^{-\frac{(\chi_n - I_n)^2}{2\sigma_n^2}}, \tag{5}$$

The intensity value of the n$^{\text{th}}$ output mode is defined as $I_n = |e_n^{(\text{out})}|^2$ where $e_n^{(\text{out})}$ is the coefficient of the n$^{\text{th}}$ output mode in the linear expansion $\mathbf{e}^{(\text{out})} = \sum_n e_n^{(\text{out})}\mathbf{y}_n$. The Fisher information then takes the following simple form

$$\mathcal{J}(\zeta) = \sum_{n=1}^{N} \frac{1}{\sigma_n^2}\left[\partial_\zeta |e_n^{(\text{out})}|^2\right]^2. \tag{6}$$

*Fisher information as a rank-one approximation.* Writing the output field in terms of the matrix $\mathbf{H}$ and the input field, which is decomposed in terms of the input modes $\{\mathbf{x}_1, \ldots, \mathbf{x}_M\}$, $\mathbf{e}^{(\text{in})} = \sum_{m=1} e_m^{(\text{in})}\mathbf{x}_m$, and normalized, $||\mathbf{e}^{(\text{in})}|| = 1$, we get that

$$\mathcal{J}(\zeta) = \frac{1}{\sigma^2}\sum_{n=1}^{N}\left[\sum_{m,m'}^{M} \partial_\zeta(\mathrm{H}_{nm}\mathrm{H}^*_{nm'}) e_m^{(\text{in})} e_{m'}^{(\text{in})*}\right]^2 \tag{7a}$$

$$= \frac{\mathcal{J}^{1/2}(\zeta)}{\sigma}\sum_{n=1}^{N}\sum_{m,m'}^{M} W^*_{nmm'} a_n e_m^{(\text{in})} e_{m'}^{(\text{in})*}, \tag{7b}$$

$$= \frac{\mathcal{J}^{1/2}(\zeta)}{\sigma}\left\langle \boldsymbol{\mathcal{W}}^{(3)}, \mathbf{a}\otimes\mathbf{e}^{(\text{in})}\otimes\mathbf{e}^{(\text{in})*}\right\rangle, \tag{7c}$$

where the real vector $\mathbf{a}$ is defined component-wise as

$$a_n = \frac{1}{\sigma\mathcal{J}^{1/2}(\zeta)}\sum_{m,m'}^{M} W_{nmm'} e_m^{(\text{in})} e_{m'}^{(\text{in})*}, \tag{8}$$

with $\|\mathbf{a}\| = \mathcal{J}^{1/2}(\zeta)$ so that it is normalized. This real vector $\mathbf{a}$ is proportional to the rate of change of the intensity distribution over the output modes with respect to the parameter $\zeta$ for the input field $\mathbf{e}^{(\text{in})}$. Its value is fixed as the one that maximizes $\mathcal{J}$ for a fixed $\mathbf{e}^{(\text{in})}$. For simplicity, we have taken the noise over the output modes to be the same, $\sigma = \sigma_n$ for all $n$, but, if needed, these output mode-dependent noise variations can be incorporated in the definition of $\boldsymbol{\mathcal{W}}^{(3)}$. Finally, by squaring both sides of Eq. 7c, the Fisher information can be rewritten as

$$\mathcal{J}(\zeta) = \frac{1}{\sigma^2}\left\langle \boldsymbol{\mathcal{W}}^{(3)}, \mathbf{a}\otimes\mathbf{e}^{(\text{in})}\otimes\mathbf{e}^{(\text{in})*}\right\rangle^2. \tag{9}$$

Maximizing $\mathcal{J}$ subject to the constraints $\|\mathbf{a}\| = ||\mathbf{e}^{(\text{in})}|| = 1$ is equivalent to the minimization problem

$$\min_{\mathbf{u},\mathbf{v},\mathbf{w}} \left\| \boldsymbol{\mathcal{W}}^{(3)} - \mathbf{u}\otimes\mathbf{v}\otimes\mathbf{w}\right\|, \text{ subject to } \frac{\mathbf{v}}{\|\mathbf{v}\|} = \frac{\mathbf{w}^*}{\|\mathbf{w}\|}, \tag{10}$$

where $\mathbf{u}$, $\mathbf{v}$ and $\mathbf{w}$ are vectors, thus showing that finding the OCC is equivalent to finding the best rank-one approximation of $\boldsymbol{\mathcal{W}}^{(3)}$ [30]. The OCC $\mathbf{e}_{\text{OCC}}^{(\text{in})}$ can then be identified from the solution as

$$\mathbf{e}_{\text{OCC}}^{(\text{in})} = \mathbf{v}/\|\mathbf{v}\|. \tag{11}$$

*Changing the OPM.* To project the output field onto a set of $Q$ orthonormal OPM, we simply apply the corresponding projection operator $\mathbf{P}$ to the output field. The projection operator satisfies $\mathbf{P}^\dagger\cdot\mathbf{P} = \mathbb{1}_Q$ where $\mathbb{1}_Q$ is the identity matrix of dimension $Q$. Note that $\mathbf{P}$ is generally not unitary since $Q$ can be less than the total number of output modes in the system. The projected output field can then be written as

$$\mathbf{e}_P^{(\text{out})} = \mathbf{P}^\dagger\cdot\mathbf{e}^{(\text{out})} = \sum_{q=1}^{Q} e_{P,q}^{(\text{out})}\mathbf{p}_q, \tag{12}$$

where $\mathbf{p}_q$ is the $q^{\text{th}}$ column of $\mathbf{P}$, i.e. the $q^{\text{th}}$ OPM, and the intensity distribution over the new OPM is given by $I_q^{(P)} = |e_{P,q}^{(\text{out})}|^2$. Rewriting the Fisher information in terms of an output modes basis that contains all the information about the output field we have that,

$$\mathcal{J}(\zeta) = \frac{1}{\sigma^2}\sum_{q=1}^{Q}\left[\partial_\zeta|e_{P,q}^{(\text{out})}|^2\right]^2, \tag{13a}$$

$$= \frac{1}{\sigma^2}\sum_{q=1}^{Q}\left[\sum_{n,n'} P^*_{nq}\partial_\zeta(e_n^{(\text{out})} e_{n'}^{(\text{out})*}) P_{n'q}\right]^2, \tag{13b}$$

$$= \frac{1}{\sigma^2}\sum_{q=1}^{Q}\langle\mathbf{p}_q, \mathbf{E}_\zeta\cdot\mathbf{p}_q\rangle^2 \tag{13c}$$

where

$$\mathbf{E}_\zeta = \partial_\zeta\left(\mathbf{e}^{(\text{out})}\otimes\mathbf{e}^{(\text{out})*}\right). \tag{14}$$

It is easy to see that the $\mathbf{E}_\zeta$ operator is Hermitian and of rank two. Therefore, it only has two non-zero eigenvalues, which means that all the information available in $\mathbf{e}^{(\text{out})}$ can be obtained by projecting into two modes. Note that this result applies even to changes happening at the source and not only those encoded in the matrix $\mathbf{H}$.

*Fisher information for optimal input-output combinations.* Now, if we want to find the optimal input-output combination in order to reach the precision limit for intensity-based measurements, then we need to write the Fisher information in terms of the input field. Moreover, as we just showed, we only need to consider projection the output into two OPM. Therefore, setting $\mathbf{e}^{(\text{out})} = \mathbf{H}\cdot\mathbf{e}^{(\text{in})}$ and $Q = 2$ in Eq. (13b), we

get

$$\mathcal{J}(\zeta) = \frac{1}{\sigma^2}\sum_{q=1}^{Q}\left[\sum_{n,n'}\sum_{mm'}\partial_\zeta(\mathrm{H}_{nm}\mathrm{H}^*_{n'm'})P^*_{nq}P_{n'q}e^{(\mathrm{in})}_m e^{(\mathrm{in})*}_{m'}\right]^2, \tag{15a}$$

$$= \frac{1}{\sigma^2}\sum_{q=1}^{Q}\langle \boldsymbol{\mathcal{W}}^{(4)}, \mathbf{p}^*_q \otimes \mathbf{p}_q \otimes \mathbf{e}^{(\mathrm{in})} \otimes \mathbf{e}^{(\mathrm{in})*}\rangle^2, \tag{15b}$$

where we defined the fourth-order tensor $\boldsymbol{\mathcal{W}}^{(4)}$ whose components are given by

$$W^{(4)}_{ijkl} = \partial_\zeta(\mathrm{H}^*_{ik}\mathrm{H}_{jl}). \tag{16}$$

## Experimental setup

The optical setup is represented in Extended Data Fig. 1. The light source consists of a continuous linearly polarized laser beam at 1550 nm (TeraXion NLL) injected into a 10:90 polarization-maintaining fiber coupler (PNH1550R2F1) in order to separate it into the shaped signal field and the reference field. The 90% arm is collimated and expanded to illuminate a digital micromirror device (DMD) (Vialux V-650L) which is used to modulate the signal field in amplitude and phase using Lee holograms [46]. The light is converted into left circular polarization using a quarter-wave plate. The shaped signal field is then imaged with a 4f system onto the input facet of a 25cm-long step-index fiber with a 50 $\mu m$ core and 0.22 numerical aperture, which is held approximately straight. The output facet is imaged via another 4f system onto an InGaAs camera (Xenics Cheetah 640-CL 400 Hz) after passing through a quarter-wave plate, followed by a beam displacer to select the left-circularly polarized component. The other 10% arm is used to produce a tilted reference that is made to interfere with the signal field in order to be able to retrieve the output field via off-axis holography [47]. An Arduino-controlled shutter allows blocking the reference field to perform intensity measurements of the signal field. The fiber can be deformed, roughly in the middle, by pressing on it using a 50 nm precision dc servo motor actuator (Thorlabs Z812). All the values reported for the deformation correspond to the linear displacement of the actuator and not the deformation of the fiber core, which is much smaller since most of the deformation is absorbed by the coating of the fiber.

## TM measurements

First, we measure the TM of the MMF in the pixel basis, by sending 7200 square layouts consisting of $37 \times 37$ square macropixels whose value is either zero or a random phase of amplitude one. Each macropixel is formed by grouping $16 \times 16$ pixels of the DMD, where the desired phase and amplitude value is encoded via Lee holograms [46] and selecting the first order of diffraction at the Fourier plane. The corresponding output fields are recovered from the interferograms between the reference and signal fields, and subsequently projected onto a square pattern of $44 \times 44$ macropixels formed by grouping $4 \times 4$ pixels of the camera. Regrouping all input and output fields into the columns of matrices $\mathbf{X}$ and $\mathbf{Y}$, respectively, we reconstruct the TM via $\mathbf{H} = \mathbf{Y} \cdot \mathbf{X}^{-1}$ where $\mathbf{X}^{-1}$ denotes the pseudoinverse of $\mathbf{X}$.

Then, we compute the SVD of the TM in the pixel basis and use it to identify the fiber modes as the singular vectors with singular values in the almost constant plateau (see Extended Data Fig. 2). For the fiber we used there were 144 fiber modes as opposed to the 129 predicted through numerical simulations. This indicates that some cladding modes are sufficiently close to the cutoff that they propagate without undergoing significant absorption for the short length we are using. All subsequent TM measurements are performed by sending 1440 random inputs obtained by randomly superimposing all 144 fiber modes. This allows us to drastically reduce the size of the TM and the higher-order tensors without losing significant information. The output fiber modes are simply the outputs generated by sending the fiber modes as inputs. These outputs are orthogonal since they correspond to the first 144 output singular vectors of the TM measured in the pixel basis.

## Optimizing the Fisher information

When the output modes are fixed, the OCC for which the Fisher information achieves a maximum can be identified from the best rank-one approximation of $\boldsymbol{\mathcal{W}}^{(3)}$. As mentioned in the main text, for matrices which are second-order tensors finding the best rank-one approximation is quite simple since one only need to compute the SVD. For tensors, it is not so simple, and thus we take a few steps to get there.

*Higher-order singular value decomposition.* A first step into the right direction can be taken by computing the HOSVD which is defined in what follows. A tensor $\boldsymbol{\mathcal{T}} \in \mathbb{C}^{I_1} \times \cdots \times \mathbb{C}^{I_L}$ of order $L$ can be decomposed as a sum of rank-one tensors using a higher-order version of the SVD,

$$\boldsymbol{\mathcal{T}} = \sum_{i_1=1}^{I_1} \cdots \sum_{i_L=1}^{I_L} s_{i_1 \cdots i_L} \mathbf{u}^{(1)}_{i_1} \otimes \cdots \otimes \mathbf{u}^{(L)}_{i_L} \tag{17}$$

where the higher-order singular vectors $\mathbf{u}^{(j)}_i$ form an orthonormal basis of $\mathbb{C}^{I_j}$, $S_{ijk}$ are the entries of the core tensor $\boldsymbol{\mathcal{S}}$, and $\otimes$ denotes the outer product. The core tensor satisfies the properties of

1. all orthogonality: $\langle \boldsymbol{\mathcal{S}}_{i_n=\alpha}, \boldsymbol{\mathcal{S}}_{i_n=\beta}\rangle = 0$ for $\alpha \neq \beta$
2. ordering: $\left\|\boldsymbol{\mathcal{S}}_{i_n=1}\right\| \geq \left\|\boldsymbol{\mathcal{S}}_{i_n=2}\right\| \geq \ldots$,

where $\langle \cdots, \cdots \rangle$ denotes the inner product induced by the Frobenius norm, namely

$$\langle \boldsymbol{\mathcal{T}}^{(1)}, \boldsymbol{\mathcal{T}}^{(2)} \rangle = \sum_{i_1=1}^{I_1} \cdots \sum_{i_L=1}^{I_L} T^{(1)\,*}_{i_1 \cdots i_L} T^{(2)}_{i_1 \cdots i_L}, \tag{18}$$

and $\boldsymbol{\mathcal{S}}_{i_n=\alpha}$ denotes the tensor obtained by setting the $n^{\text{th}}$ index equal to $\alpha$. For matrices, these properties reduce to the diagonality condition of the matrix made of singular values and their ordering.

Another important property of the HOSVD is that it preserves the partial symmetries of the original tensor, for example if $T_{i_1 \cdots i_j \cdots i_k \cdots i_L} = T^*_{i_1 \cdots i_k \cdots i_j \cdots i_L}$ then $\mathbf{u}^{(j)}_i = \mathbf{u}^{(k)*}_i$ and $S_{i_1 \cdots i_j \cdots i_k \cdots i_L} = S^*_{i_1 \cdots i_k \cdots i_j \cdots i_L}$. The biggest advantage of the HOSVD against other types of tensor decompositions is that it can be easily computed via the SVD of its matrix unfoldings

(see Refs. 31, 33 for more details). However, when truncating the HOSVD to a single term we do not get the best rank one approximation, but we do get an excellent first guess.

*Symmetrized alternating least-squares algorithm.* Finding the best rank-one approximation is a particular case of more general types of lower-rank tensor approximations based around the polyadic and Tucker decompositions [32, 34]. There are several algorithms that have been developed to find them and that could, in principle, be applied to solve the optimization problem in Eq. (10). However, most of them do not take into account the symmetries of the original tensor, and when one tries to impose them they often fail to converge.

Here, we were able to adapt the widely used alternating-least squares (ALS) algorithm in order to keep the symmetries of the original tensor. Let us consider the case of a third-order tensor $\mathcal{T}$ with partial Hermitian symmetry in the last two indices, $T_{ijk} = T^*_{ikj}$, where we seek the vectors $\mathbf{a}$ and $\mathbf{b}$ that solve

$$\min_{\mathbf{a},\mathbf{b}} \|\mathcal{T} - \mathbf{a}\otimes\mathbf{b}\otimes\mathbf{b}^*\|. \tag{19}$$

Initially, we do not force the symmetry and allow the last vector to be different, say $\mathbf{c}$ and start by minimizing $\|\mathcal{T} - \mathbf{a}\otimes\mathbf{b}\otimes\mathbf{c}\|$. We proceed as a standard ALS routine by fixing $\mathbf{b}$ and $\mathbf{c}$, and solving the minimization problem

$$\min_{\mathbf{a}} \|\mathcal{T} - \mathbf{a}\otimes\mathbf{b}\otimes\mathbf{c}\|, \tag{20}$$

which is a standard least-squares problem with a fixed solution. Then, we do the same for $\mathbf{b}$ and $\mathbf{c}$. Before performing another loop, we symmetrize the lower rank tensor by setting

$$\mathbf{b} \leftarrow \frac{\sqrt{\|\mathbf{b}\|\|\mathbf{c}\|}}{2}\left(\frac{\mathbf{b}}{\|\mathbf{b}\|} + \frac{\mathbf{c}^*}{\|\mathbf{c}\|}\right) \tag{21}$$

$$\mathbf{c} \leftarrow \mathbf{b}^* \tag{22}$$

This simple adaptation gives enough freedom so the algorithm converges and provides a solution with the desired symmetry. A similar approach is taken to compute the rank-one approximation of $\mathcal{W}^{(4)}$.

The ALS algorithm requires us to provide it with a starting point, that is a first guess for the best rank-one approximation. Here, we use as a seed the rank-one tensor obtained by truncating the HOSVD to a single term. This choice allows us to systematically converge to the optimal solution whereas when using a random guess there is a high probability to fall into a local minimum.

*Finding the optimal input-output combination.* The first step in finding the optimal input-output combination is to compute the fourth-order tensor $\mathcal{W}^{(4)}$. Given the number of pixels used as output modes to measure $\mathbf{H}$, the size of this tensor would be too large to be useful for computations. However, since the number of input modes is much lower, one can see that using all the 1444 output pixels might be an overkill. Therefore, we first compute the SVD for the two TMs that we used to compute $\mathcal{W}^{(3)}$ and use their output singular vectors to form an orthonormal set of output modes. This new set of output modes has double the number of input modes used, but it allows us to capture all the information encoded in the pixel basis but at a much smaller size. Then, we project the TMs onto this set of output modes and use this projected TMs to compute $\mathcal{W}^{(4)}$.

As mentioned in the main text, when trying to find the optimal input-output combination that allows reaching the precision limit, the Fisher information given by Eq. (3) no longer takes the form of a lower-rank tensor decomposition. Nonetheless, it is possible to rewrite it as a nonlinear optimization where only the expansion coefficients of the input field in terms of the input modes are used as optimization parameters. This is done by first computing the output field using the TM, then getting the optimal OPMs and using those to compute the Fisher information. This optimization was implemented using the neural network framework PyTorch. Here again, we need to provide a first guess, and, as for the ALS algorithm, we chose to use the first term of the HOSVD of $\mathcal{W}^{(4)}$.

## Experimental estimation of the deformation

*Noise characterization.* Before performing the experimental estimation of small deformations, we need to verify the veracity of the assumption of Gaussian noise made in this work for our setup. For this, we performed a set of characterization measurements for two values of the input power and the four fields used to perform the estimation. The first one was performed at the highest input power possible without saturating any pixels of the camera and taking care to send the same amount of energy for each input field. The second one was performed using only 20% of the total power used for the first one. For each set, we sent 500 copies of the four fields and used the measured output intensity distributions to compute the mean and standard deviation value of the intensity over the output pixels as shown in Extended Data Fig. 3. At higher power we can clearly see some intensity-dependent behavior in the standard deviation which is used to characterize the noise, particularly for the OCC for which the focal spot is clearly visible. At lower power, however, this dependence on the intensity for the noise is almost completely gone with the $\sigma_n$ values being fairly uniform. These results confirm that our assumption of Gaussian noise are valid particularly at the powers used to perform the estimation.

*Estimating the deformation.* Given that the perturbations under consideration are small, it is sensible to assume a linear model for the measured intensity distribution $\boldsymbol{\chi}$ over the output modes after a change $\Delta\xi$ in the perturbation. Explicitly, we have that

$$\boldsymbol{\chi} \approx \mathbf{I}(\zeta_i) + \mathbf{I}_\zeta(\zeta_i)\Delta\zeta + \boldsymbol{w}(\sigma), \tag{23}$$

where $\mathbf{I}(\zeta_i)$ represents the output intensity distribution over the output modes prior to changing the deformation, $\mathbf{I}_\zeta(\zeta_i)$ is the derivative of $\mathbf{I}$ with respect to $\zeta$ and evaluated at $\zeta_i$, and $\boldsymbol{w}(\sigma)$ is a vector of normally distributed independent random variables with zero mean and standard deviation $\sigma$. For this linear model the minimum variance unbiased estimator [25] is given by

$$\Delta\zeta^{(\mathrm{est})}(\boldsymbol{\chi}) = \frac{\mathbf{I}_\zeta(\zeta_i)\cdot[\boldsymbol{\chi} - \mathbf{I}(\zeta_i)]}{\left\|\mathbf{I}_\zeta(\zeta_i)\right\|^2}. \tag{24}$$

In this model, both the reference intensity distribution $\mathbf{I}$ and the derivative $\partial_\zeta\mathbf{I}$ are assumed to be known. To calibrate the

derivative, we first set the input power as high as possible without saturating any pixels for any of the fields used for the estimation. Then, we perform 500 independent measurements for each field and for two deformations centered around the reference value $\zeta_i$. Then, the derivative of the intensity distribution of each field is estimated by taking the difference between the mean for each deformation and dividing by the total deformation performed between the two points. As can be seen in Extended Data Fig. 4, the distribution of the mean change in intensity obtained from these calibration measurements is quite smooth, even though the effect of noise is noticeable for each individual realization, and with its main values above the noise level shown in Extended Data Fig. 3 for all the fields. Also shown in Extended Data Fig. 4 are the distribution of the mean change in intensity and a single realization at the input power used for the estimation of the smallest change. Here, we can see that each individual change is quite susceptible to noise and that its effect is even noticeable for the mean distribution, particularly for the worst performing field given by the random wavefront. For the reference intensity distribution, we can use the same input power used for the estimations since the mean intensity distribution is well above the noise level for all fields (see Extended Data Fig. 3). Moreover, using the same input power for the reference as for the estimation allows the nonuniform background to be automatically removed.

## Data availability

Examples of the data can be found in the dedicated GitHub repository [48]. All other datasets used in this work are available from the authors upon reasonable request.

## Code availability

All the code used to produce the results and figures presented in this work can be found in the dedicated GitHub repository [48].

## References

[46] W.-H. Lee. III computer-generated holograms: Techniques and applications. In *Progress in Optics*, pp. 119–232 (Elsevier, 1978).

[47] E. Cuche, P. Marquet and C. Depeursinge. Spatial filtering for zero-order and twin-image elimination in digital off-axis holography. *Appl. Opt.* **39** no. 23, pp. 4070–4075 (2000).

[48] R. Gutiérrez-Cuevas. Crashingdisorder. https://github.com/rodguti90/CrashingDisorder.

## Acknowledgements

R. G. C. acknowledges L. L. Sánchez-Soto and K. Liang for useful discussions.

## Author contributions

R.G.C. conceived the project, developed the theory and performed the experimental measurements. S.M.P. supervised the experimental work and theory development. All authors contributed to the scientific discussion and the writing of the manuscript.

## Funding

The authors acknowledge the French Agence Nationale pour la Recherche (Grant No. ANR-20-CE24-0016 MUPHTA) and the Labex WIFI (ANR-10-LABX-24, ANR-10-IDEX-0001-02 PSL*).

## Competing interests

The authors declare no competing interests.

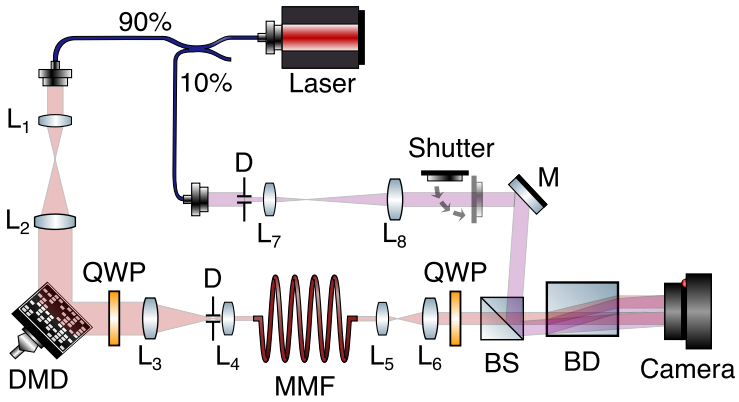


**Extended Data Figure 1 | Optical setup.** DMD, digital micromirror device; $L_i$, lenses; QWP, quarter-wave plates; M, mirror; D, diaphragm; BD, beam displacer; BS, beam splitter. The shutter is used to block the reference beam in order to perform intensity measurements.

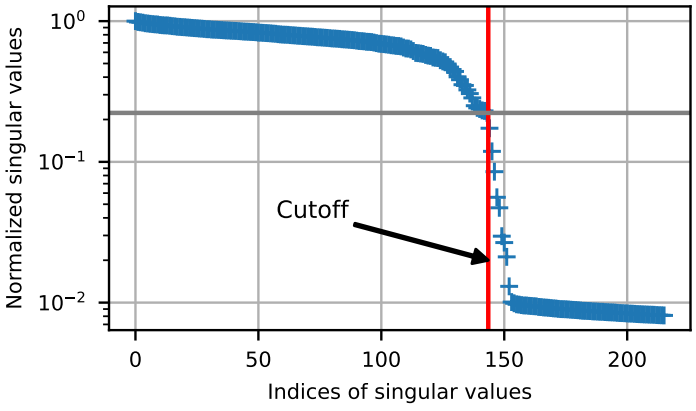


**Extended Data Figure 2 | Identifying the fiber modes.** Singular values of the TM measured in the pixel basis. The fiber modes are identified as the singular vectors for which the singular values light in the plateau. The cutoff value is marked by the vertical red line.

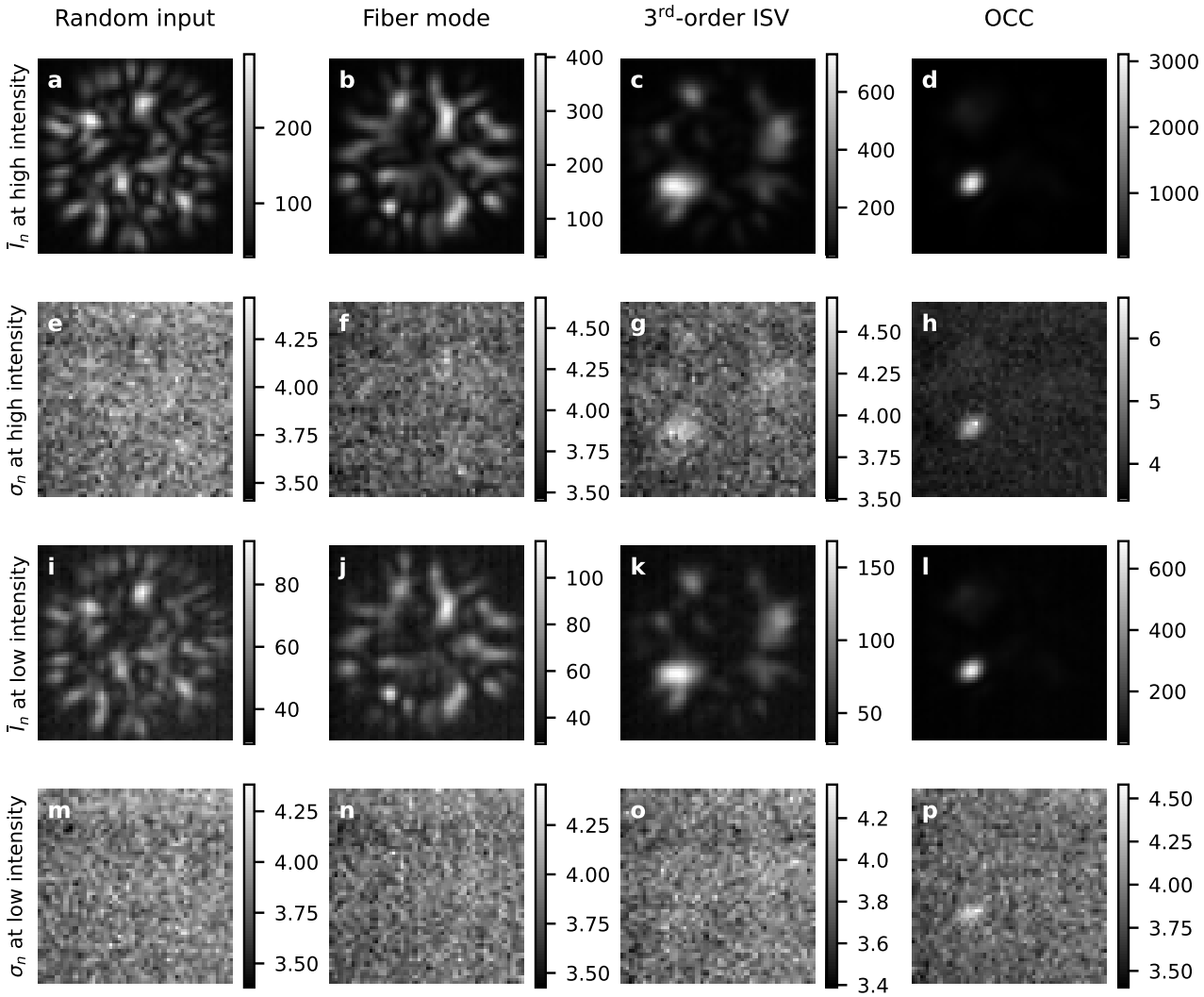


**Extended Data Figure 3 | Noise characterization. a-d,i-l,** Mean intensity distributions and **e-h,m-p,** standard deviations for the four fields used for the parameter estimation at high-intensity values (**a-h**) and when only 20% of the light is sent (**i-p**).

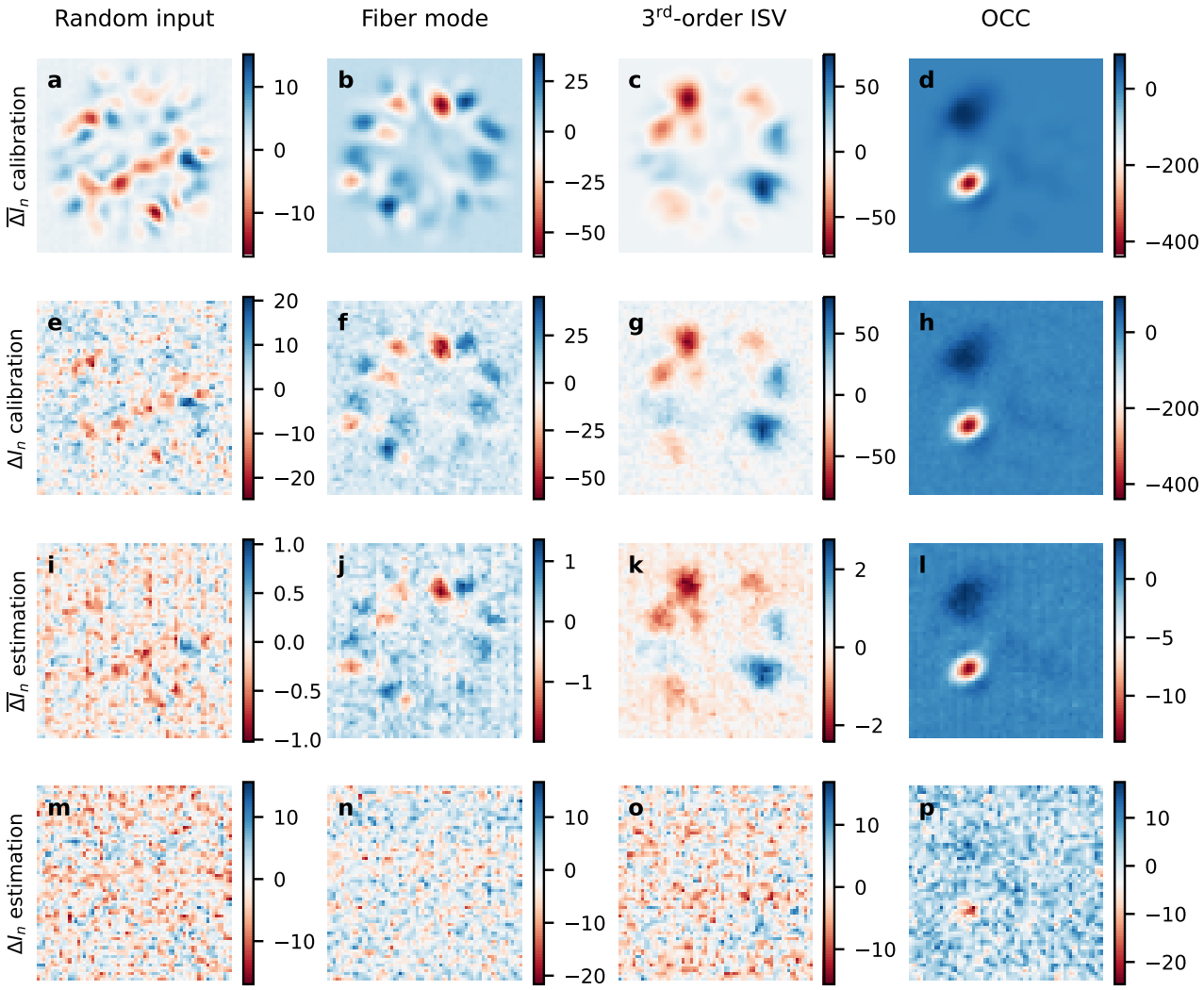


**Extended Data Figure 4 | Change in intensity. a-d,i-l,** Mean and **e-h,m-p,** single change in intensity distributions for the four fields used to calibrate the derivative and acquired at high-intensity values (**a-h**), and those used to estimate the smallest deformation when using only 20% of the light sent for the calibration (**i-p**).